Halobenzene Clathrates of the Porous Metal−Organic Spin-Crossover Framework [Fe(tvp)$_2$(NCS)$_2$]$_n$. Stabilization of a Four-Step Transition

Alejandro Orellana-Silla, Francisco Javier Valverde-Muñoz,* M. Carmen Muñoz, Carlos Bartual-Murgui, Sacramento Ferrer, and José Antonio Real*

Read Online

| ACCESS | 📊 Metrics & More | 📖 Article Recommendations | 🅢ℹ Supporting Information |

ABSTRACT: Here we show that the porous metal−organic spin crossover (SCO) framework [Fe(tvp)$_2$(NCS)$_2$]@4(CH$_3$CN·H$_2$O) [**1@4(CH$_3$CN·H$_2$O)**] is an excellent precursor material for the systematic synthesis, via single-crystal to single-crystal transformation, of a series of halobenzene clathrates. Immersion of samples constituted of single crystals of **1@4(CH$_3$CN·H$_2$O)** in the liquid halobenzenes PhX$_n$, X = F (n = 1−6), X = Cl (n = 1, 2), and X = Br (n = 1) at room temperature induces complete replacement of the guest molecules by PhX$_n$ to afford **1@2PhX$_n$**. Single-crystal analyses of the new clathrates confirm the integrity of the porous framework with the PhX$_n$ guests being organized by pairs via π-stacking filling the nanochannels. The magnetic and calorimetric data confirm the occurrence of practically complete SCO behavior in all of the clathrates. The characteristic SCO equilibrium temperatures, $T_{1/2}$, seem to be the result of a subtle balance in the host−guest interactions, which are temperature- and spin-state-dependent. The radically distinct supramolecular organization of the PhCl$_2$ guests in **1@2PhCl$_2$** affords a rare example of four-step SCO behavior following the sequence [HS$_1$:LS$_0$] ↔ [HS$_{2/3}$:LS$_{1/3}$] ↔ [HS$_{1/2}$:LS$_{1/2}$] ↔ [HS$_{1/4}$:LS$_{3/4}$] ↔ [HS$_0$:LS$_1$], which has been structurally characterized.
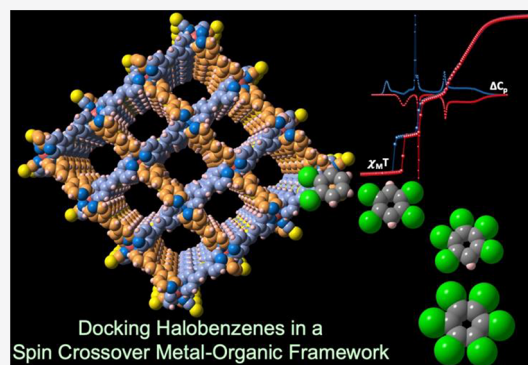
INTRODUCTION

Octahedral Fe^{II} spin-crossover complexes are a singular class of electronically labile materials reversibly switching between the high (HS, t$_{2g}^4$e$_g^2$) and low (LS, t$_{2g}^6$e$_g^0$) spin states in response to temperature, pressure, light irradiation, and interaction with guest molecules. The HS ↔ LS switch is accompanied by noticeable changes in the magnetic, electrical, and optical properties of the material. Furthermore, due to the antibonding nature of the e$_g$ orbitals, their population− depopulation is strongly coupled to structural changes involving metal to ligand bond lengths and angles, resulting in an expansion−contraction of the coordination octahedron. In the crystalline state, the change in size of the Fe^{II} octahedron is the source of the elastic stress responsible for cooperativity, which critically depends on the coupling between the Fe^{II} centers mediated by intermolecular interactions.[1−9] Strong coupling favors abrupt HS ↔ LS transitions accompanied in favorable cases by hysteretic behavior, which confers a memory effect to the SCO material. In absence of antagonistic elastic stresses in the crystal, the HS ↔ LS transition occurs in one step while the presence of elastic frustration[10−12] divides the HS ↔ LS transformation into successive steps (two, three, or more) as a mechanism to minimize the energy cost of the transformation, thereby conferring multistability (three or more steps) to the

material.[13−23] The possibility of controlling the HS ↔ LS switching at macro-, micro-, and nanometric levels has created important possibilities for technological applications.[24−26]

Among the Fe^{II} SCO complexes, coordination polymers have long attracted much interest because they represent an excellent opportunity to explore different strategies for coupling SCO centers and thus understand the mechanisms that control the cooperativity.[6,27−33] This interest was significantly increased with the first porous SCO coordination polymers reported, since they additionally afforded the prospect of investigating the impact of host−guest interactions on the SCO properties. In this context, the family of doubly interpenetrated two-dimensional Fe^{II} SCO coordination polymers generically formulated as [Fe(L)$_2$(NCS)$_2$]@Guest, L being the bis-monodentate pyridine-type bridging ligands tvp (*trans*-(4,4′-vinylenedipyridine)),[34] azpy (4,4′-azopyridine),[35] bpbd (2,3-bis(4′-pyridyl)-2,3-butanediol),[36,37] bpe (1,2-bis(4′-
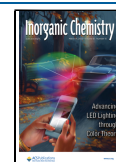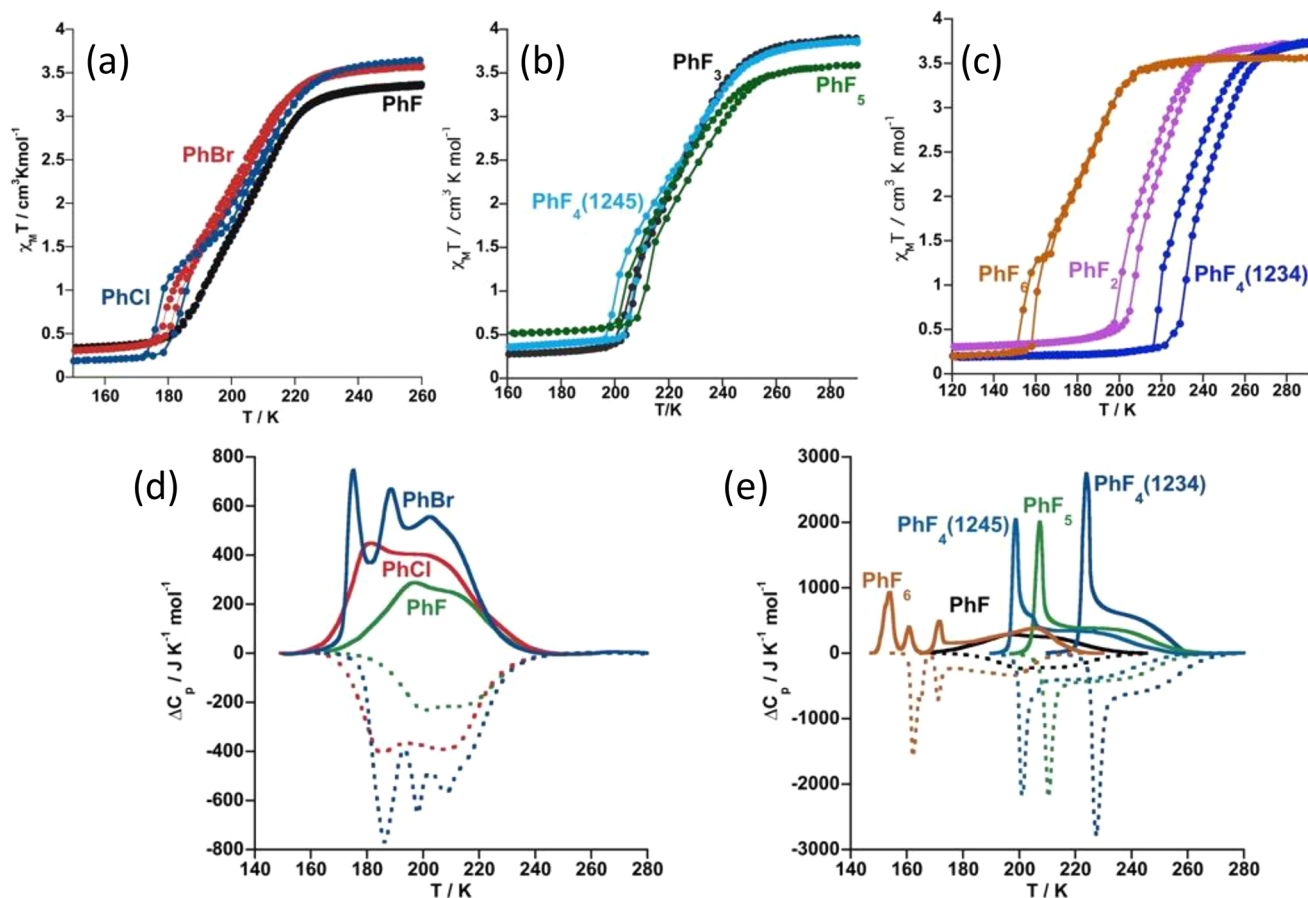
Figure 1. Thermal dependence of $\chi_M T$ (a−c) and ΔC_p (d, e) for **1@2PhX$_n$**. Solid and dotted lines in (d) and (e) correspond to the cooling and heating modes, respectively.

pyridyl)ethane),[38] and bped (*dl*-1,2-bis(4′-pyridyl)-1,2-ethane-diol)[39] has had a pivotal influence on the field. Recently, a number of clathrates of the type [Fe(tvp)$_2$(NCS)$_2$]@Guest (**1@G**) were reported with a variety of guests such as water, acetonitrile, dimethylacetamide, dimethylsulfoxide, benzonitrile, benzaldehyde, and nitrobenzene.[40] From this study, we realized that the **1@4(CH$_3$CN·H$_2$O)** clathrate afforded large, robust, and rather stable single crystals in relatively good yield. Thus, we decided to investigate this material as a precursor for systematic syntheses of new clathrate homologues via a single-crystal to single-crystal (SCSC) procedure. For this study, we selected a series of halogeno-benzene derivatives (PhX$_n$: X = Cl (*n* = 1, 2); X = F (*n* = 1–3, 4 (two isomers), 5, 6); X = Br (*n* = 1)) as suitable guests, since they are liquids at room temperature. Thus, here we report the synthesis, via an SCSC procedure, the structures and physical characterizations of the corresponding clathrates generically formulated as **1@xPhX$_n$**. The structural, magnetic, and calorimetric data confirm that all of the clathrates show complete LS ↔ HS transitions. The clathrate **1@2PhCl$_2$** undergoes an uncommon four-step SCO behavior that seems to be correlated with the different orientation of the aromatic guests docked in the channels.

■ RESULTS

Synthesis and Thermal Stability. The starting single crystals of the precursor **1@4(CH$_3$CN·H$_2$O)** were prepared by liquid–liquid diffusion in test tubes.[40] The corresponding species **1@2PhX$_n$** were prepared by soaking single crystals of

1@4(CH$_3$CN·H$_2$O) in pure liquids of **PhX = PhF, Ph(1,2)-F$_2$, Ph(1,2,3)-F$_3$, Ph(1,2,3,4)-F$_4$, Ph(1,2,4,5)-F$_4$, PhF$_5$, PhF$_6$, PhCl, Ph(1,2)-Cl$_2$, and PhBr** for the required time to replace the CH$_3$CN and H$_2$O molecules from the channels of **1**. Thermogravimetric analyses (TGA) of freshly prepared single crystals reveal that all compounds decompose in three well-defined steps (Figure S1). A first step, involving the loss of two molecules of PhX$_n$, takes place in the interval 300−450 K, being centered at ca. 380−448 K depending on the derivative. Then a second step centered at ca. 480−540 K follows, involving a loss of weight consistent with one molecule of tvp, and finally, the third step centered at ca. 605−650 K involves the loss of the second tvp ligand and two SCN groups, the remaining mass being reasonably consistent with a residue of FeO at around 800 K (Figure S1). All of the guests are stable inside the pores except for the lightest ones, i.e. PhCl, PhF$_x$ (*x* = 1, 2 and 3), and PhBr, which are loosely attached to the walls of the channels and gradually desorb with time (see also the single-crystal section). For example, **1@2PhF** loses ca. 19% of its weight in 2 days, consistent with the desorption of 1.4 molecules of PhF. This effect markedly decreases with an increase in the molecular weight of the guest: e.g., the losses of weight for the homologous PhCl and PhBr clathrates in the same period are ca. 6.2% (∼0.45 molecule) and 5% (∼0.3 molecule), respectively (see Figure S2). However, elemental analyses of freshly prepared samples of these derivatives support the presence of two guest PhX$_n$ molecules, similarly to the stable members of the series, a fact also confirmed by the
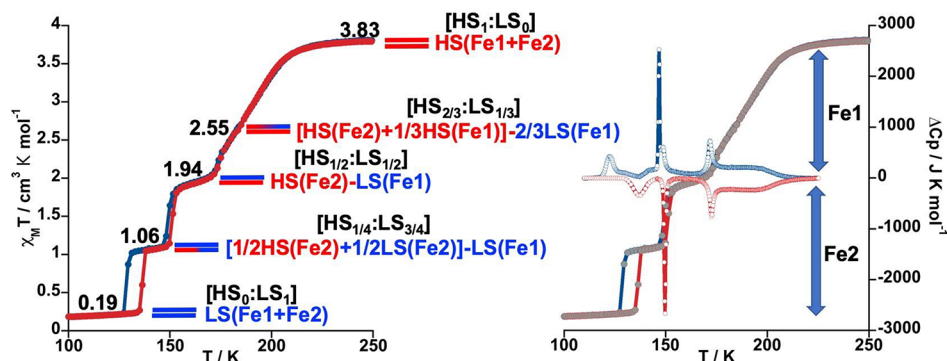
Figure 2. SCO properties of **1@2PhCl₂**. (left) Thermal dependence of $\chi_M T$. Horizontal bars represent the evolution of the spin state (LS blue/HS red) for the two crystallographically distinct Fe1 and Fe2 centers. (right) Overlay of the thermal dependence of ΔC_p and $\chi_M T$ plots.
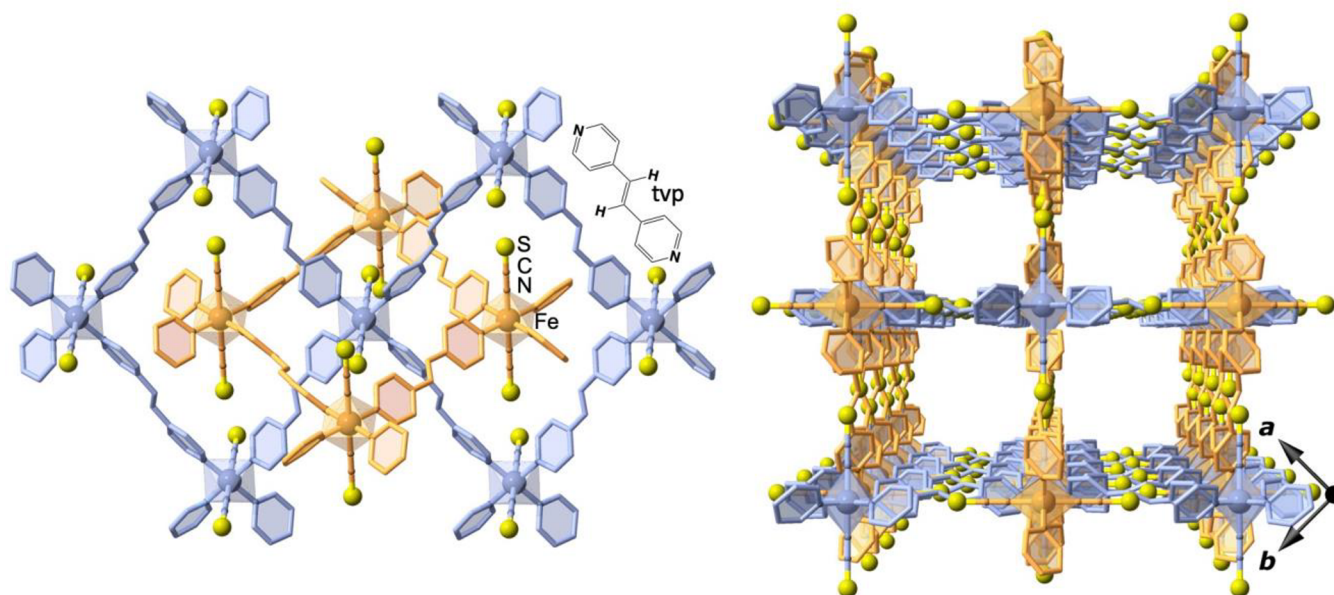
Figure 3. (left) View of two orthogonally interpenetrated $[\text{Fe(tvp)}_2(\text{NCS})_2]_n$ layers emphasizing the pseudo-octahedral coordination environment of the Fe^{II} nodes and their relative orientation. (right) Perspective view down the c direction of the stacking of the two different sets of layers defining wide square-shaped channels. Yellow spheres represent the S atoms of the SCN⁻ groups. The two independent orthogonally interlocked stacks of layers are shown in orange and blue.

crystal structure of the PhCl₂ and PhF$_n$ (n = 4−6) clathrates (see the next sections).

Spin-Crossover Behavior. The SCO properties of freshly prepared crystals of **1@2PhX$_n$** were analyzed from the thermal dependence of the $\chi_M T$ product and ΔC_p, where χ_M is the molar magnetic susceptibility monitored using a SQUID susceptometer (T scan rates 1−2 K/min), T is the temperature, and ΔC_p represents the variation of the anomalous specific heat capacity derived from differential scanning calorimetry (T scan rates 5−10 K/min) (see the Experimental Section). $\chi_M T$ and ΔC_p vs T plots are displayed in Figures 1 and 2 (DSC vs T plots for **1@2PhF$_n$**, n = 2, 3, are shown in Figure S3).

At room temperature, the $\chi_M T$ product (3.39−3.86 cm³ K mol⁻¹) is in the range typically observed for an Fe^{II} center in the HS state. Upon cooling, $\chi_M T$ remains almost constant above a certain interval of temperatures but then decreases, first gradually at intermediate temperatures and then more abruptly at lower temperatures, reaching values in the range 0.08−0.25 cm³ K mol⁻¹, which involves HS molar fractions between ca. 0% and 6%, indicating that the SCO is practically

complete (Figure 1a−c). The clathrate **1@2PhCl₂** displays a four-step SCO associated with the presence of two crystallographically distinct Fe^{II} centers (Fe1 and Fe2; see structure) and average characteristic temperatures defined by the maxima described by $\partial(\chi_M T)/\partial T$ centered at ca. T_c = 192 K (first), 173 K (second), 150 K (third) and 132 K (fourth), which correspond reasonably well to the switches between the states [HS₁:LS₀] ↔ [HS$_{2/3}$:LS$_{1/3}$] ↔ [HS$_{1/2}$:LS$_{1/2}$] ↔ [HS$_{1/4}$:LS$_{3/4}$] ↔ [HS₀:LS₁] defined by the $\chi_M T$ intervals 3.83 ↔ 2.55 ↔ 1.94 ↔ 1.06 ↔ 0.19 cm³ K mol⁻¹, respectively (Figure 3). Except for the PhF derivative, the $\chi_M T$ vs T plot in the heating mode does not match that of the cooling mode, particularly in the abrupt part of the SCO at low temperatures, thereby defining a narrow asymmetric thermal hysteresis in the interval range 2−10 K. The average equilibrium temperature, $T_{1/2}^{av}$, at which the molar fractions of the HS and LS states, γ_{HS} and γ_{LS}, are equal to 0.5 (where the variation of the free energy $\Delta G = 0$) is shown in Table 1 for all derivatives. These $T_{1/2}^{av}$ values have been calculated by taking into account that $(\chi_M T)_{1/2} = \{[(\chi_M T)_{HT} - (\chi_M T)_{LT}]/2\} + (\chi_M T)_{LT}$, $(\chi_M T)_{HT}$ and $(\chi_M T)_{LT}$ being the $\chi_M T$ values at high (ca. 280−300 K) and low- (ca.

Table 1. Thermodynamic Parameters for 1@2PhX$_n$

clathrate	$T_{1/2}{}^{av}$/K	ΔH^{av}/kJ mol^{-1}	ΔS^{av}/J K^{-1} mol^{-1}
1@2PhCl	198	19.01	96.0
1@2PhCl$_2$	162	16.86	104.1
1@2PhF	203	9.67	47.7
1@2PhF$_2$	213	18.62	87.4
1@2PhF$_3$	220	21.91	99.6
1@2PhF$_4$(1,2,3,4)	235	26.63	113.3
1@2PhF$_4$(1,2,4,5)	217	21.98	101.3
1@2PhF$_5$	220	22.78	103.5
1@2PhF$_6$	175	17.21	98.4
1@2PhBr	200	24.0	120.0

100 K) temperatures, where the compounds are practically HS and LS, respectively.

The thermal dependence of ΔC_p, in the cooling and heating modes, reflects reasonably well the SCO behavior described by the magnetic measurements. The wide shoulder dominating the high-temperature range corresponds to the more gradual part of the SCO (smaller slope), while the sharp maximum at lower temperatures reflects the increase of slope in the $\chi_M T$ vs T curve. The four steps described for the PhCl$_2$ derivative from the $\chi_M T$ vs T plot are quite well reproduced by the ΔC_p vs T plot. For each compound, the average variations of enthalpy, ΔH^{av}, obtained from integration of the area below the ΔC_p vs T curves and the corresponding average variations of entropy calculated as $\Delta S^{av} = \Delta H^{av}/T_{1/2}{}^{av}$ are gathered in Table 1. These enthalpy and entropy values are in general larger than those usually observed for Fe^{II} SCO compounds but are consistent with those observed for previously reported clathrates of the porous framework [Fe(tvp)$_2$(NCS)$_2$]$_n$.[40]

Structure of 1@xPhX$_n$. Single-crystal analyses were carried out for all the clathrates under study using freshly prepared samples. The lightest guests of the **1@2PhX$_n$** series, PhCl and PhF$_n$ (n = 1, 2, 3), were found to be strongly disordered and the diffuse electron density could not be modeled. The scattering contributions of the disordered guests were removed using the solvent mask procedure implemented in Olex2.[41] The electron density evaluated by following this protocol suggests that the amount of guest in the pores is reduced by ca. 25–40%, presumably favored by the continuous N$_2$ jet during the single-crystal X-ray diffraction measurements, giving the estimated content of guest $x \approx 1.14$–1.32. In contrast, **1@2PhCl$_2$** and the more hightly substituted fluorobenzene guests, n = 4–6, were perfectly localized in the channels. Despite this, the R value for the clathrate **1@2PhF$_4$(1,2,4,5)** (R_{int} = 0.13) is surprisingly high, most probably due to fractures in the crystals or twinning. However, the data have sufficient quality to allow an accurate determination of the structure of both the host framework and the guests. Only the cell parameters could be obtained for **1@xPhBr** (see Table S1).

Except for **1@2PhCl$_2$**, all of the structures investigated are centrosymmetric. The PhX$_n$ derivatives with X = F, Cl, Br are isostructural and display the tetragonal space group $P4/ncc$, while the remaining centrosymmetric clathrates adopt the orthorhombic space group $Pccn$. The noncentrosymmetric PhCl$_2$ derivative adopts the space group $P\bar{4}2_1c$ in the whole range of temperatures measured and contains two enantiomeric forms. All of the clathrate compounds show the same basic structure for the metal–organic framework,[6,11] the main difference being the guest molecule and its location in the channels. Crystallographic data for the **1@xPhX$_n$** series are

gathered in Tables S2–S4 while Tables S5–S7 contain a selection of relevant bond lengths and angles.

Let us recall the structure of the centrosymmetric porous host frameworks. It is constituted of a unique type of pseudo-octahedral Fe^{II} site which defines the nodes of the framework. Each Fe^{II} node is equatorially connected to four adjacent equivalent nodes lying in the same plane through four bis-bidentate tvp bridging ligands, while two terminal SCN$^-$ groups complete the axial positions of the octahedron. The resulting 2D layered [Fe(tvp)$_2$(NCS)$_2$]$_n$ coordination polymers define two independent and orthogonally interpenetrated stacks giving large square-shaped channels that confer a porous nature to the compound (Figure 3).

The structures **1@xPhX$_n$** with X = Cl ($x \approx 1.2$, n = 1), F ($x \approx 1.1$–1.3, n = 1–3), and F (x = 2, n = 5) were analyzed at 140/260 K (PhCl), 130/260 K (PhF), 140/263 K (PhF$_2$), and 120/260 K (PhF$_3$ and PhF$_5$), where the compounds are in the LS/HS state. In the HS state the average Fe–N bond length $\langle$Fe–N$\rangle_{av}$ is serially 2.170(4), 2.171(4), 2.158(3), 2.170(3) and 2.156(7) Å and shortens 0.194, 0.200, 0.181, 0.199, and 0.189 Å down to 1.976(3), 1.971(4), 1.977(2), 1.971(3), and 1.967(4) Å in the LS state. The apparent partial loss of the guest in four of the five clathrates does not significantly affect the variations of $\langle$Fe–N$\rangle_{av}$, since they are perfectly consistent with what is expected for a complete HS $\leftrightarrow$ LS conversion, in agreement with the magnetic behavior. In this respect, it is worth pointing out again that complete loss of the guest induces stabilization of the HS state for the empty framework.[40] Then, below a certain threshold value of x for the aforementioned derivatives it is expected that the incompleteness of the SCO will grow more and more as x approaches zero. For the derivatives **1@2PhF$_n$** with n = 4 (1,2,3,4- and 1,2,4,5-isomers) and n = 6 the structures were measured at 120 K, giving respectively $\langle$Fe–N$\rangle_{av}$ bond lengths of 1.974(2), 1.971(6) and 1.991(8) Å, typical of the LS state.

Because of the multistep SCO nature of **1@2PhCl$_2$**, its structure was analyzed at four characteristic temperatures (105, 140, 160, and 250 K), which correspond to the well-defined plateaus between the successive steps. The poorly marked plateau and its pronounced slope prevented us from analyzing it at around 194 K, which corresponds to a ca. HS$_{2/3}$:LS$_{1/3}$ state (see Figure 2, left). The structure of the host framework is essentially the same as for the rest of the **1@xPhX$_n$** family, but in contrast, there are two crystallographically distinct Fe^{II} pseudo-octahedral centers (Fe1 and Fe2) (Table S5) featuring practically the same $\langle$Fe–N$\rangle_{av}$ values, 1.980(4) Å (Fe1) and 1.983(4) Å (Fe2), at 105 K. The only remarkable difference is observed for the angular distortion parameters $\sum$(Fe$_i$) (sum of the deviation from 90° of the 12 cis angles of the [FeN$_6$] octahedron), which are 10.68 and 7.45° for Fe1 and Fe2, respectively. Upon heating, the Fe1 site remains within the typical limits of the LS state ($\langle$Fe1–N$\rangle_{av}$ = 1.982(3) Å (140 K) and 1.991(3) Å (160 K)), while for the Fe2 site $\langle$Fe2–N$\rangle_{av}$ substantially increases by 0.092 Å (140 K) and 0.084 Å (160 K) up to 2.074(3) and 2.158(3) Å, respectively. The $\sum$ parameter slightly increases for Fe1 (to 11.21 and 11.83°) and increases more markedly for Fe2 (to 8.85 and 10.57°) upon heating to 140 and 160 K, respectively. At 250 K, the $\langle$Fe1–N$\rangle_{av}$ value increases by 0.185 Å up to 2.176(5) Å, while an additional increase of 0.023 Å is observed for $\langle$Fe2–N$\rangle_{av}$ to reach a final value of 2.181(5) Å. At 250 K, $\sum$ values are 13.92 and 12.07° for Fe1 and Fe2, respectively. The global $\langle$Fe(1+2)–N$\rangle_{av}$ average values move following the sequence
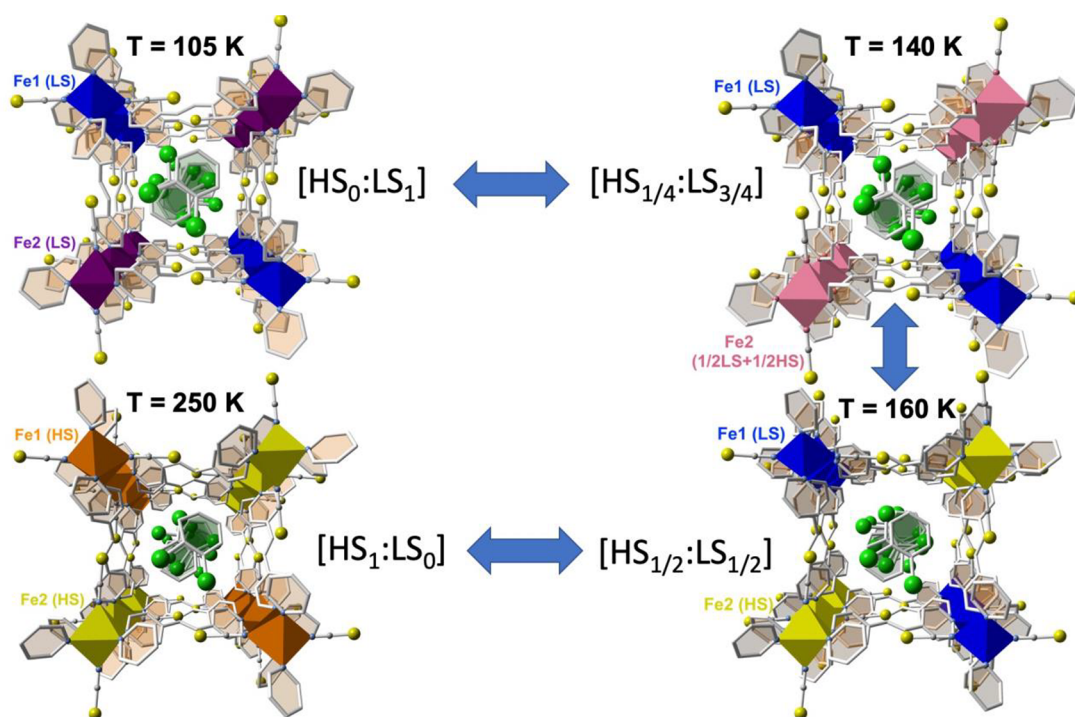
Figure 4. Fragment of the structure of **1@2PhCl₂** showing the guest PhCl₂ molecules in the middle of the channels and the spin-state change of the Fe^{II} octahedral nodes. Color codes: Fe1 (LS), blue; Fe2 (LS), garnet; Fe2 (HS), yellow; Fe1 (HS), brown; Fe2 (1/2HS+1/2LS), pink.

1.981(4) Å (105 K), 2.028(3) Å (140 K), 2.074(3) Å (160 K), and 2.178(5) Å (250 K). These results indicate that the differences in $\langle$Fe−N$\rangle_{av}$ between the HS and LS states, 0.196 Å (Fe1), 0.198 Å (Fe2), and 0.197 Å (Fe1 + Fe2), are consistent with the occurrence of complete SCO and, the sequence of changes in $\langle$Fe−N$\rangle_{av}$, $\langle$Fe1−N$\rangle_{av}$, and $\langle$Fe2−N$\rangle_{av}$ agree reasonably with the sequence deduced from the $\chi_M T$ vs T plot for **1@2PhCl₂**. Although from the structural data no ordering was observed for the distribution of the LS and HS Fe2 centers at 140 K, it is reasonable to suggest that they alternate parallel to c, as shown in Figure 4 (pink octahedra).

The clathrates exhibiting low- or medium-disordered guest molecules, i.e. **1@2PhF$_n$** with n = 4 (1,2,3,4- and 1,2,4,5-substituted), 5, 6 and **1@2PhCl₂**, clearly show the guest aromatic rings filling the nanochannels organized in a more or less displaced face to face fashion held together through π−π interactions. In the LS state, the centroid to centroid separations are respectively 3.568 and 3.417, 3.533, and 3.493 Å for the tetra (1,2,3,4 and 1,2,4,5)- penta-, and hexasubstituted **1@2PhF$_n$** derivatives and 3.575 Å for **1@2PhCl₂**. This separation increases by 0.158 and 0.089 Å upon switching from the LS to the HS state for **1@2PhF₅** and **1@2PhCl₂**, respectively.

It is important to note that the packing of the guest pairs in **1@2PhCl₂** is radically distinct from that found for the remaining members of the series. Indeed, the PhCl₂ aromatic rings are practically parallel-oriented to the cross-section surface defined by the nanochannels, while the other PhX$_n$ rings of the series are perpendicularly oriented to it (see Figure 5 and Figure S4). Consequently, the smallest centroid to centroid separation between two consecutive pairs is shorter for **1@2PhCl₂** (5.607 Å (LS) and 5.457 Å (HS)), these separations being in the interval 7.861−8.242 Å (LS state) for the fluorine derivatives. Despite this, the effective separation between the **PhF$_n$** (n = 4−6) rings is determined by the
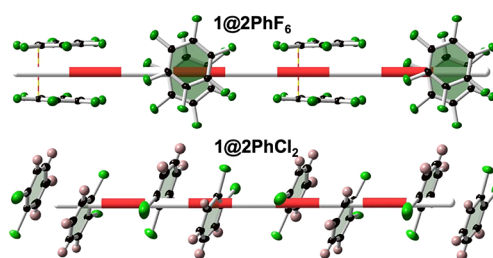
Figure 5. Supramolecular organization of the guests in the nanochannels running along the z direction for **1@PhF₆** and **1@PhCl₂**. The large bicolor bar denotes the center of the pore. The thin bicolor line in **1@PhF₆** corresponds to the shortest C···C intermolecular distance, 3.239 Å, smaller than the sum of the van der Waals radii (3.4 Å).

shortest F···F distances between consecutive pairs (3.135 Å (n = 6), 3.255 Å (LS)/3.337 Å (HS) (n = 5), 3.277 Å (n = 4 (1,2,3,4)), and 3.364 Å (n = 4 (1,2,4,5))), which are somewhat larger than the sum of the van der Waals radii (2.94 Å).

The singular orientation of the guests in **1@2PhCl₂** determines the nature of the shortest intermolecular host−guest contacts, involving additional Cl···C and Cl···S close distances at 105 K where the two Fe^{II} centers are in the LS state (d(Cl1···C19) = 3.410 Å; d(Cl2···C6) = 3.380 Å, and d(Cl3···S1) = 3.559 Å) (Figure 6, left). In contrast, only the most crowded derivatives of the PhF$_n$ series, i.e. **1@2PhF₆** and **1@2PhF₅**, display two and one host−guest S···C contact (S···C14 = 3.401 Å and S···C15 = 3.488 Å at 150 K and S···C15 = 3.485 Å, 120 K, respectively) (Figure 6, right, and Figure S5); for the rest of the members these contacts are larger than the sum of the van der Waals radii. A common feature of all the members of the [Fe(tvp)₂(NCS)₂@Guest] family is the occurrence of two characteristic host−host C···S interactions in the LS state between the S atom of the NCS⁻ groups of one
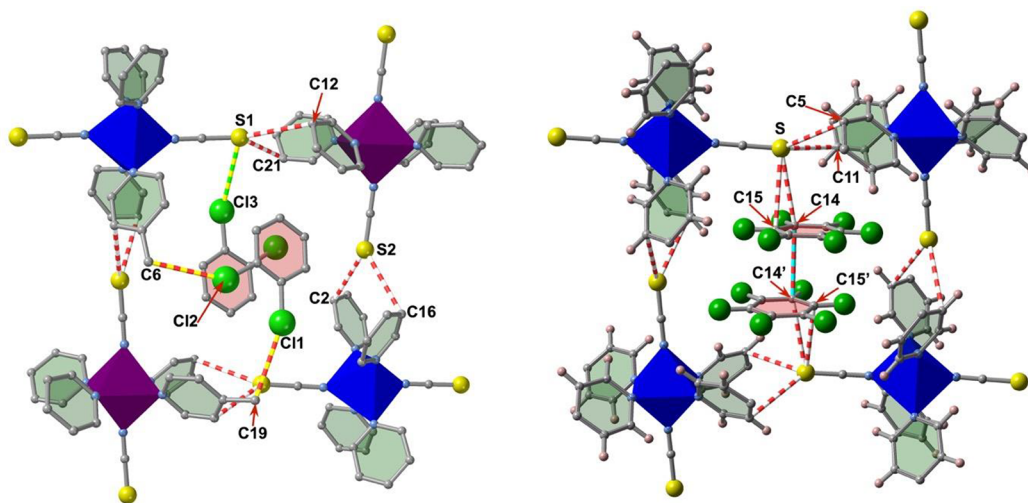
Figure 6. Representative guest−guest (blue−red), host−guest (green−yellow) and host−host (red−white) intermolecular contacts for the LS structures of **1@2PhCl₂** (104 K) (left) and **1@2PhF₆** (120 K) (right).

independent stack of layers and two C atoms of two "cis" pyridines belonging to the other independent interpenetrated stack of layers (see Figure 6 and Figure S5). All of these interactions gradually weaken as the HS is populated (Figure S6).

DISCUSSION AND CONCLUSIONS

We reinvestigate here the clathration properties of the host system $[Fe(tvp)_2(NCS)_2]_n$ (**1**) made up of two mutually interpenetrated orthogonal stacks of parallel 2D layers, which afforded the first example of porous SCO.[34] More precisely, the aim of this study was first to demonstrate the reliability of the **1@4(H₂O·CH₃CN)** derivative as a precursor for the systematic synthesis of halogeno-benzene clathrates by interchanging the H₂O and CH₃CN molecules via single-crystal to single-crystal transformations. This has been achieved by soaking the precursor crystals in the liquid of the appropriate guest PhX$_n$ (X = F, Cl, Br; n = 1−6). The second aim was to investigate the SCO properties of the resulting new clathrates.

With regard to the first aspect, the results clearly show that **1@4(H₂O·CH₃CN)** is an excellent starting material to obtain high-quality single crystals of the selected halogeno-benzene clathrates **1@2PhX$_n$** in good yield. Despite this, the lightest PhX$_n$ members of the series (PhCl and PhF$_n$ (n = 1−3)) are loosely attached to the walls of the channels of the host **1** and tend to escape. Although this circumstance has not prevented the standard characterization of the corresponding clathrate compounds, it has a marked effect on the single-crystal X-ray measurements, this being the cause of the low nominal loading of guest molecules inferred from the single-crystal analysis. In addition, it contributes to an increase in the high disorder observed for the confined guests, a fact that does not allow us to describe neither their orientation in the channels nor the potential host−guest and guest−guest short contacts. A similar situation was previously reported for the PhCHO and PhNO₂ clathrates.[40] However, a picture of the supramolecular organization for the PhCHO molecules has been recently obtained from molecular dynamics simulations,[41] which agrees reasonably well with the distribution in the channels of a homologous PhCN clathrate directly observed from a single-crystal analysis[40] (see Figure S7) as well as in the clathrates **1@**

2PhF$_n$ (n = 4−6), described here, and in the p-dichlorobenzene clathrate of the equivalent orthogonally interpenetrated 2D framework $[Fe(bpe)_2(NCS)_2]_n$.[38c]

As their congeners **1@4(H₂O·CH₃CN)** and **1@2PhCN**, the simplest **1@xPhX** (1 ≤ x ≤ 2; X = F, Cl, Br) clathrates crystallize in the space group P4/ncc under ambient conditions, where the HS state is stable. However, while **1@xPhX** retains this space group in a switch to the LS state, the first two undergo a crystallographic phase transition, adopting the space group Pccn that involves a change in the crossing angle defined by the interpenetrated 2D frameworks from orthogonal to oblique. In contrast, despite the layers remaining orthogonally interpenetrated, the space group Pccn is also observed in the LS state for **1@xPhF$_n$** (n = 2−6). Whatever the space group, the precise supramolecular organizations adopted by the distinct halogeno-benzene molecules in the host channels do not substantially differ from each other and are slightly modulated by the size and number of substituents in the benzene ring, with the remarkable exception of **1@2PhCl₂**. In this case the benzene rings adopt a parallel disposition with respect to the square cross-section of the channels, in contrast to the other members of the series (including **1@2PhCN** and **1@2PhCHO**), which adopt a perpendicular disposition.

The halobenzene clathrates here reported display complete SCO behavior with more or less marked differences both in the characteristic $T_{1/2}$ temperatures and in the thermal evolution of the HS/LS population, somewhat modulated by the nature and disposition of the guest in the channels. With regard to the freshly prepared single halogenated benzenes **1@2PhX** (X = F, Cl, Br), the change from F to Br does not significantly influence the $T_{1/2}$ value, lying in the range 198−203 K (see Table 1) but promotes simultaneously an increase in cooperativity and the emergence of hysteresis as well as an incipient new SCO step at low temperatures. The hysteresis and the step are not present for the F derivative but are apparent and become more noticeable on moving from Cl to Br (see Figure S8). Both features are also obvious for the **1@2PhF$_n$** (n = 2−6) derivatives. Furthermore, except for **1@2PhF₆** characterized by $T_{1/2}$ = 175 K, the rest of the series display somewhat larger $T_{1/2}$ values (range 213−235 K) in comparison to those observed for the single halogenated benzenes. All of these observations derived from the $\chi_M T$ vs T

plots are reasonably well supported by the DSC measurements, which confirm the occurrence at least two incipient steps.

Although it was much less marked in comparison with the title compounds, the propensity of SCO to occur in two steps with different cooperativities was already noted previously for the clathrates 4($H_2O \cdot CH_3CN$), 2PhNO$_2$, and 2PhCHO. This was associated with the accommodation of the framework and guests to the changes in bond lengths and bond angles of the [$Fe^{II}N_6$] core produced during the thermally induced SCO. As a consequence, the underlying structural constraints generate intermediate phases that evolve with the degree of HS ↔ LS transformation, a fact that is consistent with the characteristic high ΔH and ΔS values obtained for the majority of the members of the **1@Guest** family. In particular, up to three structural phases have been identified for **1@2PhCHO** in a recent detailed study, mentioned above, that combines variable-temperature synchrotron X-ray diffraction measurements (to determine the long-range order and symmetry lowering) and molecular dynamics simulations (to explore the structure of the guest confined in the channels).[42]

Coming back to the $T_{1/2}$ values, we observed no clear correlation in the series of **1@2PhF$_n$** (n = 1−6). Only in the case of **1@2PhF$_6$**, the fact of showing the lowest $T_{1/2}$ value of the series clearly seems to be correlated with additional short host−guest contacts taking place between the S atom of the SCN$^-$ groups and the C14 (3.401 Å) and C15 (3.488 Å) atoms of the most voluminous guest PhF$_6$ (Figure 6, right). Obviously, these additional contacts condition the capability of the host framework **1** to self-adapt to the dimensions imposed by the LS state, thereby inducing elastic constraints that destabilize the LS state, pushing down $T_{1/2}$. Contacts between equivalent atoms are slightly larger for the other members of the series and depend on the exact location of the pairs (PhF$_n$)$_2$ in the channels, which is modulated by the number of F atoms and their distribution in the ring. These subtle differences are the only features that may explain the observed $T_{1/2}$ values for the remaining members of the series. Connected with this are the singular properties observed for **1@2PhCl$_2$**. Its average $T_{1/2}$ value is even smaller than that of **1@2PhF$_6$**, a fact that is a consequence of the special disposition adopted by the PhCl$_2$ rings in the channels, partially blocking the breathing mode of the host framework and hence destabilizing the LS state. This is supported by the fact that the separation between the aromatic rings of a pair of π−π interacting guests (PhCl$_2$)$_2$ shrinks upon the HS ↔ LS transformation ca. 56% less (0.089 Å) than was observed for the opposite docking configuration of the (PhX$_n$)$_2$ pairs adopted by the other members of the series, in particular for **1@2PhF$_5$**. In this system, the separation between the PhF$_5$ rings in the pairs (PhX$_5$)$_2$ decreases 0.158 Å. As a consequence, **1@2PhCl$_2$** undergoes an uncommon four-step SCO behavior, three of which have been structurally characterized. The steps correspond to the energy tolls required to overcome the elastic frustration generated by the shortest intermolecular short contacts between the host framework and the PhCl$_2$ guests. It is worth noting that no symmetry breaking has been observed at the temperatures investigated. Indeed, the correlation of spin state and structure for the three structurally characterized steps is compatible with the presence of two different Fe^{II} sites, each one residing separately in one of the two orthogonally interpenetrated stacks of 2D layers. During the switching from the [LS$_0$−HS$_1$] to the [LS$_{1/2}$−HS$_{1/2}$] state, only the stack containing the Fe1 site adopts the LS, while the subsequent

steps to the [LS$_{3/4}$−LS$_{1/4}$] and [LS$_1$−HS$_0$] states each involve half of the Fe2 centers. Despite the well-defined plateau generated by the [LS$_{3/4}$−HS$_{1/4}$] state, no Fe2(LS)−Fe2(HS) order is observed, only an average value between both Fe2 sites. Most likely, this order would require a change in space group that is not observed. Although we have not analyzed the structure of the poorly defined step consistent with the [HS$_{2/3}$−LS$_{1/3}$] state at around 192 K, surely it is subjected to similar constraints. The occurrence of multistepped SCO behavior has recently attracted much attention not only for fundamental reasons, since it provides the possibility to find correlations between different competing elastic interactions in the crystal and the stabilization of ordered [LS$_i$−HS$_j$] spin states, but also for practical reasons, since these states could be used to design more advanced complex memories. So far, the number of SCO complexes exhibiting well-documented four-step SCO behavior is small. Indeed, to the best of our knowledge, the examples are limited to nine and all of them are coordination polymers.[14,16−22] From these examples, it can be inferred that in all of them the stabilization of the intermediate states/steps depends on the presence of subtle elastic interactions stemming from supramolecular short contacts that in turn critically depend on the specific composition of the sample. The difficult control of the intermolecular interactions makes the multistepped SCO behavior a fortuitous event and only the systematic search for suitable new SCO compounds will afford the control of these interactions, the rational design of the SCO-steps and possible applications in the future.

■ EXPERIMENTAL SECTION

Materials and Reagents. *trans*-(4,4′-Vinylenedipyridine), iron-(II) sulfate heptahydrate, potassium thiocyanate, and all of the halobenzenes employed here were obtained from commercial sources and used as received without further purification.

Synthesis of 1@4(MeCN·H$_2$O). This compound was synthesized following a literature procedure.[40] A slow liquid−liquid diffusion technique (layering) using standard test tubes was used to obtain samples of the precursor **1@4(MeCN·H$_2$O)** constituted essentially of single crystals. The bottom layer contains a mixture of FeSO$_4$·7H$_2$O (75 mg, 0.27 mmol) and KNCS (52.3 mg, 0.54 mmol) in 5 mL of water, the middle layer is a 1/1 H$_2$O/MeCN mixture (10 mL), and the top layer contains a MeCN solution of tvp (98.3 mg, 0.54 mmol) (5 mL). All manipulations were performed under an Ar atmosphere, and the solutions contained very small quantities of ascorbic acid to prevent oxidation of the Fe^{II} ion. Anal. Calcd for C$_{34}$H$_{40}$N$_{10}$O$_4$S$_2$Fe: C, 52.86; H, 5.18; N, 18.14. Found: C, 53.04; H, 5.11; N, 17.95.

Synthesis of 1@2PhX$_n$. The halobenzene clathrates were synthesized by soaking single crystals of **1@4(CH$_3$CN·H$_2$O)** (ca. 50 mg) in ca. 3 mL of PhX$_n$ (PhF, Ph(1,2)-F$_2$, Ph(1,2,3)-F$_3$, Ph(1,2,3,4)-F$_4$, Ph(1,2,4,5)-F$_4$, PhF$_5$, PhF$_6$, PhCl, Ph(1,2)-Cl$_2$, and PhBr) for ca. 10 days. It is important to note that, depending on the relative density of the guest with respect to that of the precursor crystals, the procedure was slightly modified. For PhX$_n$ guests less dense than the crystals, the solid−liquid mixture was kept, usually, in small closed vials. However, in the opposite case, to keep the crystals submerged in the liquid it was necessary to use a syringe as a vial closed with a rubber stopper, as shown in Figure S9. The liquid of the mixtures was replaced every day to accelerate the exchange of guests. Freshly prepared samples of **1@2PhX$_n$** were used for elemental analyses. Anal. Calcd for C$_{38}$H$_{30}$F$_2$N$_6$FeS$_2$ (**1@2PhF**): C, 62.64; H, 4.15; N, 11.53. Found: C, 51.07; H, 3.92; N, 11.07). Calcd for C$_{38}$H$_{28}$F$_4$N$_6$FeS$_2$ (**1@2PhF$_2$**): C, 59.69; H, 3.69; N, 10.99. Found: C, 58.83; H, 3.61; N, 10.65. Calcd for C$_{38}$H$_{26}$F$_6$N$_6$FeS$_2$ (**1@2PhF$_3$**): C, 57.01; H, 3.27; N, 10.50. Found: C, 56.35; H, 3.16; N, 10.28. Calcd for C$_{38}$H$_{24}$F$_8$N$_6$FeS$_2$ (**1@2PhF$_4$** [1,2,3,4]): C, 54.56; H, 2.89; N, 10.05. Found: C, 54.11; H, 2.82; N, 9.89. Calcd for C$_{38}$H$_{24}$F$_8$N$_6$FeS$_2$

(**1@2PhF$_4$** [1,2,4,5]): C, 54.56; H, 2.89; N, 10.05. Found: C, 54.08; H, 2.75; N, 9.94. Calcd for C$_{38}$H$_{22}$F$_{10}$N$_6$FeS$_2$ (**1@2PhF$_5$**): C, 52.31; H, 2.54; N, 9.63. Found: C, 51.89; H, 2.49; N, 9.56. Calcd for C$_{38}$H$_{20}$F$_{12}$N$_6$FeS$_2$ (**1@2PhF$_6$**): C, 50.23; H, 2.22; N, 9.25. Found: C, 49.87; H, 2.19; N, 9.17. Calcd for C$_{38}$H$_{30}$Cl$_2$N$_6$FeS$_2$ (**1@2PhCl**): C, 59.93; H, 3.97; N, 11.04. Found: C, 58.41; H, 3.66; N, 10.53. Calcd for C$_{38}$H$_{28}$Cl$_4$N$_6$FeS$_2$ (**1@2PhCl$_2$**): C, 54.96; H, 3.56; N, 9.88. Found: C, 58.41; H, 3.66; N, 10.53. Calcd for C$_{38}$H$_{30}$Br$_2$N$_6$FeS$_2$ (**1@2PhCl**): C, 53.67; H, 3.56; N, 9.88. Found: C, 52.90%; H, 3.49; N, 9.72.

Physical Measurements. *Magnetic Measurements.* Variable temperature magnetic susceptibility data were recorded with a Quantum Design MPMS2 SQUID magnetometer equipped with a 7 T magnet, operating at 1 T and at temperatures of 1.8−400 K. Experimental susceptibilities were corrected for diamagnetism of the constituent atoms by the use of Pascal's constants.

Calorimetric and Thermogravimetric Measurements. Differential scanning calorimetry measurements were performed using a Mettler Toledo Model DSC 821e calorimeter. Low temperatures were obtained with an aluminum block attached to the sample holder, refrigerated with a flow of liquid nitrogen, and stabilized at a temperature of 110 K. The sample holder was kept in a drybox under a flow of dry nitrogen gas to avoid water condensation. The measurements were performed using ~15 mg of microcrystalline samples of **1@2PhX$_n$** sealed in aluminum pans with a mechanical crimp. Temperature and heat flow calibrations were made with standard samples of indium by using its melting transition (429.6 K, 28.45 J g^{-1}). An overall accuracy of ±0.2 K in temperature and ±2% in the heat capacity is estimated. The uncertainty increases for the determination of the anomalous enthalpy and entropy due to the subtraction of an unknown baseline.

Thermogravimetric analysis was performed on a Mettler Toledo TGA/SDTA 851e instrument, in the 290−1200 K temperature range under a nitrogen atmosphere at a rate of 10 K min^{-1}.

Single-Crystal X-ray Diffraction. Single-crystal X-ray data were collected on an Oxford Diffraction Supernova diffractometer using graphite-monochromated Mo Kα radiation (λ = 0.71073 Å). A multiscan absorption correction was performed. The structures were solved by direct methods using SHELXS-2014 and refined by full matrix least-squares on F^2 using SHELXL-2014.[43] Non-hydrogen atoms were refined anisotropically, and hydrogen atoms were placed in calculated positions, refined using idealized geometries (riding model), and assigned fixed isotropic displacement parameters. The following CCDC file numbers contain supplementary crystallographic data for this article. **1@1.2PhCl**: CCDC 2130154 (140 K) and CCDC 2130155 (260 K). **1@2PhCl$_2$**: CCDC 2130159 (105 K), CCDC 2130158 (140 K), CCDC 2130166 (160 K), and CCDC 2130165 (250 K). **1@1.3PhF**: CCDC 2130162 (130 K) and CCDC 2130157 (260 K). **1@1.14PhF$_2$**: CCDC 2130156 (140 K). **1@1.2PhF$_3$**: CCDC 2130163 (150 K). **1@2PhF$_4$(1,2,3,4)**: CCDC 2130160 (150 K). **1@2PhF$_4$(1,2,4,5)**: CCDC 2130161 (150 K). **1@2PhF$_5$**: CCDC 2130168 (120 K) and CCDC 2130164 (260 K). **1@2PhF$_6$**: CCDC 2130167 (120 K).

ASSOCIATED CONTENT

Ⓢ Supporting Information

The Supporting Information is available free of charge at https://pubs.acs.org/doi/10.1021/acs.inorgchem.2c00014.

> Thermogravimetric analyses, differential scanning calorimetry, details of the crystal data collection and refinement parameters as well as selected bond distances and angles, supramolecular organization and supramolecular short contacts, perspective view of the structure of **1@2PhCN**, thermal dependence of $\chi_M T$ for **1@2PhX** (X = F, Cl, Br), and experimental setup for PhX$_n$ guests denser than **1@4(CH$_3$CN·H$_2$O)** (PDF)

Accession Codes

CCDC 2130154−2130168 contain the supplementary crystallographic data for this paper. These data can be obtained free of charge via www.ccdc.cam.ac.uk/data_request/cif, or by emailing data_request@ccdc.cam.ac.uk, or by contacting The Cambridge Crystallographic Data Centre, 12 Union Road, Cambridge CB2 1EZ, UK; fax: +44 1223 336033.

■ AUTHOR INFORMATION

Corresponding Authors

Francisco Javier Valverde-Muñoz − *Instituto de Ciencia Molecular/Departamento de Química Inorgánica, Universidad de Valencia, 46980 Valencia, Spain;* Email: francisco.valverde@uv.es

José Antonio Real − *Instituto de Ciencia Molecular/Departamento de Química Inorgánica, Universidad de Valencia, 46980 Valencia, Spain;* ⊚ orcid.org/0000-0002-2302-561X; Email: jose.a.real@uv.es

Authors

Alejandro Orellana-Silla − *Instituto de Ciencia Molecular/Departamento de Química Inorgánica, Universidad de Valencia, 46980 Valencia, Spain*

M. Carmen Muñoz − *Departamento de Física Aplicada, Universitat Politècnica de València, 46022 Valencia, Spain;* ⊚ orcid.org/0000-0003-2630-3897

Carlos Bartual-Murgui − *Instituto de Ciencia Molecular/Departamento de Química Inorgánica, Universidad de Valencia, 46980 Valencia, Spain;* ⊚ orcid.org/0000-0003-1547-8018

Sacramento Ferrer − *Departamento de Química Inorgánica, Universidad de Valencia, 46100 Valencia, Spain;* ⊚ orcid.org/0000-0001-7820-671X

Complete contact information is available at:
https://pubs.acs.org/10.1021/acs.inorgchem.2c00014

Author Contributions

All authors have given approval to the final version of the manuscript.

Notes

The authors declare no competing financial interest.

■ REFERENCES

(1) König, E. Nature and dynamics of the spin-state interconversion in metal complexes. *Struct. Bonding (Berlin)* **1991**, *76*, 51−152.

(2) Gütlich, P.; Hauser, A.; Spiering, H. Thermal and optical switching of iron(II) complexes. *Angew. Chem., Int. Ed.* **1994**, *33*, 2024−2054.

(3) Gütlich, P.; Goodwin, G. Spin crossover in transition metal compound I-III. *Topics in Current Chemistry* **2004**, *235*, 233−235.

(4) Real, J. A.; Gaspar, A. B.; Muñoz, M. C. Thermal pressure and light switchable spin-crossover materials. *Dalton Trans.* **2005**, 2062−2079.

(5) Halcrow, M. A. The spin-states and spin-transitions of mononuclear iron(II) complexes of nitrogen-donor ligands. *Polyhedron* **2007**, *26*, 3523−3576.

(6) Weber, B. Spin crossover complexes with N4O2 coordination sphere-The influence of covalent linkers on cooperative interactions. *Coord. Chem. Rev.* **2009**, *253*, 2432−2449.

(7) Aromí, G.; Barrios, L. A.; Roubeau, O.; Gamez, P. Triazoles and tetrazoles: Prime ligands to generate remarkable coordination materials. *Coord. Chem. Rev.* **2011**, *255*, 485−546.

(8) Bousseksou, A., Ed. Spin Crossover Phenomenon, *C. R. Chimie* **2018**, *21*, 1055−1299.

(9) Hogue, R. W.; Singh, S.; Brooker, S. Spin crossover in discrete polynuclear iron(II) complexes. *Chem. Soc. Rev.* **2018**, *47*, 7303−7338.

(10) (a) Paez-Espejo, M.; Sy, M.; Boukheddaden, K. Elastic frustration causing two-step and multistep transitions in spin-crossover solids: Emergence of complex antiferroelastic structures. *J. Am. Chem. Soc.* **2016**, *138*, 3202−3210. (b) Traiche, R.; Sy, M.; Boukheddaden, K. Elastic frustration in 1D spin-crossover chains: Evidence of multi-step transitions and selforganizations of the spin states. *J. Phys. Chem. C* **2018**, *122*, 4083−4096.

(11) (a) Cruddas, J.; Powell, B. J. Spin-state ice in elastically frustrated spin-crossover materials. *J. Am. Chem. Soc.* **2019**, *141*, 19790−19799. (b) Cruddas, J.; Powell, B. J. Structure−property relationships and the mechanisms of multistep transitions in spin crossover materials and frameworks. *Inorg. Chem. Front.* **2020**, *7*, 4424−443.

(12) Popa, A.-I.; Stoleriu, L.; Enachescu, C. Tutorial on the elastic theory of spin crossover materials. *J. Appl. Phys.* **2021**, *129*, 131101−131124.

(13) Sciortino, N. F.; Scherl-Gruenwald, K. R.; Chastanet, G.; Halder, G. J.; Chapman, K. W.; Létard, J.-F.; Kepert, C. J. Hysteretic three-step spin crossover in a thermo- and photochromic 3D pillared Hofmann-type metal-organic framework. *Angew. Chem., Int. Ed.* **2012**, *51*, 10154−10158.

(14) (a) Trzop, E.; Zhang, D.; Piñeiro-Lopez, L.; Valverde-Muñoz, F. J.; Muñoz, M. C.; Palatinus, L.; Guerin, L.; Cailleau, H.; Real, J. A.; Collet, E. First step towards a devil's staircase in spin-crossover materials. *Angew. Chem., Int. Ed.* **2016**, *55*, 8675−8679. (b) Zhang, D.; Trzop, E.; Valverde-Muñoz, F. J.; Piñeiro-López, L.; Muñoz, M. C.; Collet, E.; Real, J. A. Competing phases involving spin-state and ligand structural orderings in a multistable two-dimensional spin crossover coordination polymer. *Cryst. Growth Des.* **2017**, *17*, 2736−2745.

(15) Murphy, M. J.; Zenere, K. A.; Ragon, F.; Southon, P. D.; Kepert, C. J.; Neville, S. M. Guest programmable multistep spin crossover in a porous 2-D Hofmann-type material. *J. Am. Chem. Soc.* **2017**, *139*, 1330−1335.

(16) Sciortino, N. F.; Zenere, K. A.; Corrigan, M. E.; Halder, G. J.; Chastanet, G.; Létard, J.-F.; Kepert, C. J.; Neville, S. M. Four-step iron(II) spin state cascade driven by antagonistic solid state interactions. *Chem. Sci.* **2017**, *8*, 701−707.

(17) Clements, J. E.; Price, J. R.; Neville, S. M.; Kepert, C. J. Hysteretic four-step spin crossover within a three-dimensional porous Hofmann-like material. *Angew. Chem., Int. Ed.* **2016**, *55*, 15105−15109.

(18) Liu, W.; Peng, Y.-Y.; Wu, S.-G.; Chen, Y.-C.; Hoque, Md. N.; Ni, Z.-P.; Chen, X.-M.; Tong, M.-L. Guest-switchable multi-step spin transitions in an amine-functionalized metal-organic framework. *Angew. Chem., Int. Ed.* **2017**, *56*, 14982−14986.

(19) Zhang, C.-J.; Lian, K.-T.; Wu, S.-G.; Huang, G.-Z.; Ni, Z.-P.; Tong, M.-L. The substituent guest effect on four-step spin crossover behavior. *Inorg. Chem. Front.* **2020**, *7*, 911−917.

(20) Zhang, C.-J.; Lian, K.-T.; Huang, G.-Z.; Bala, S.; Ni, Z.-P.; Tong, M.-L. Hysteretic four-step spin-crossover in a 3D Hofmann-type metal−organic framework with aromatic guest. *Chem. Commun.* **2019**, *55*, 11033−11036.

(21) Peng, Y.-Y.; Wu, S.-G.; Chen, Y.-C.; Liu, W.; Huang, G.-Z.; Ni, Z.-P.; Tong, M.-L. Asymmetric seven-/eight-step spin-crossover in a three-dimensional Hofmann-type metal−organic framework. *Inorg. Chem. Front.* **2020**, *7*, 1685−1690.

(22) Piñeiro-López, L.; Valverde-Muñoz, F.-J.; Trzop, E.; Muñoz, M. C.; Seredyuk, M.; Castells-Gil, J.; da Silva, I.; Martí-Gastaldo, C.; Collet, E.; Real, J. A. Guest induced reversible on−off switching of elastic frustration in a 3D spin crossover coordination polymer with room temperature hysteretic behavior. *Chem. Sci.* **2021**, *12*, 1317−1326.

(23) Li, Z.-Y.; Dai, J.-W.; Shiota, Y.; Yoshizawa, K.; Kanegawa, S.; Sato, O. Multi-Step Spin Crossover Accompanied by Symmetry Breaking in an Fe^{III} Complex: Crystallographic Evidence and DFT Studies. *Chem. - Eur. J.* **2013**, *19*, 12948−12952.

(24) Manrique-Juárez, M. D.; Rat, S.; Salmon, L.; Molnár, G.; Quintero, C. M.; Nicu, L.; Shepherd, H. J.; Bousseksou, A. Switchable molecule-based materials for micro- and nanoscale actuating applications: achievements and prospects. *Coord. Chem. Rev.* **2016**, *308*, 395−408.

(25) Senthil Kumar, K.; Ruben, M. Emerging trends in spin crossover (SCO) based functional materials and devices. *Coord. Chem. Rev.* **2017**, *346*, 176−205.

(26) Molnár, G.; Rat, S.; Salmon, L.; Nicolazzi, W.; Bousseksou, A. Spin crossover nanomaterials: from fundamental concepts to devices. *Adv. Mater.* **2018**, *30*, No. 1703862.

(27) Kahn, O.; Martinez, J. Spin-transition polymers: from molecular materials toward memory devices. *Science* **1998**, *279*, 44−48.

(28) Real, J. A.; Gaspar, A. B.; Niel, V.; Muñoz, M. C. Communication between iron(II) building blocks in cooperative spin transition phenomena. *Coord. Chem. Rev.* **2003**, *236*, 121−141.

(29) Garcia, Y.; Niel, V.; Muñoz, M. C.; Real, J. A. Spin crossover in 1D, 2D and 3D polymeric Fe(II) networks. *Top. Curr. Chem.* **2004**, *233*, 229−257.

(30) Muñoz, M. C.; Real, J. A. Thermo-, piezo-, photo- and chemo-switchable spin crossover Iron(II) metallocyanate based coordination polymers. *Coord. Chem. Rev.* **2011**, *255*, 2068−2093.

(31) Muñoz, M. C., Real, J. A. In *Spin-crossover materials properties and applications*; Halcrow, M. A., Ed.; Wiley: 2013; pp 121−146.

(32) Ni, Z. P.; Liu, J. L.; Hoque, M. N.; Liu, W.; Li, J. Y.; Chen, Y. C.; Tong, M. L. Recent advances in guest effects on spin-crossover behavior in Hofmann-type metal-organic frameworks. *Coord. Chem. Rev.* **2017**, *335*, 28−43.

(33) Galán Mascarós, J. R.; Aromí, G.; Darawsheh, M. Polynuclear Fe(II) complexes: di/trinuclear molecules and coordination polymers. *C. R. Chimie* **2018**, *21*, 1209−1229.

(34) Real, J. A.; Andrés, E.; Muñoz, M. C.; Julve, M.; Granier, T.; Bousseksou, A.; Varret, F. Spin crossover in a catenane supra-molecular system. *Science* **1995**, *268*, 265−267.

(35) Halder, G. J.; Kepert, C. J.; Moubaraki, B.; Murray, K. S.; Cashion, J. D. Guest-dependent spin crossover in a nanoporous molecular framework material. *Science* **2002**, *298*, 1762−1765.

(36) Neville, S. M.; Moubaraki, B.; Murray, K. S.; Kepert, C. J. A thermal spin transition in a nanoporous iron(II) coordination framework material. *Angew. Chem., Int. Ed.* **2007**, *46*, 2059−2062.

(37) Neville, S. M.; Halder, G. J.; Chapman, K. W.; Duriska, M. B.; Moubaraki, B.; Murray, K. S.; Kepert, C. J. Guest tunable structure and spin crossover properties in a nanoporous coordination framework material. *J. Am. Chem. Soc.* **2009**, *131*, 12106−12108.

(38) (a) Morita, T.; Asada, Y.; Okuda, T.; Nakashima, S. Isomerism of assembled iron complex bridged by 1,2-di(4-pyridyl)ethane and its solid-to-solid transformation accompanied by a change of electronic state. *Bull. Chem. Soc. Jpn.* **2006**, *79*, 738−744. (b) Halder, G. J.; Chapman, K. W.; Neville, S. M.; Moubaraki, B.; Murray, K. S.; Létard, J.-F.; Kepert, C. J. Elucidating the mechanism of a two-step spin transition in a nanoporous metal-organic framework. *J. Am. Chem. Soc.* **2008**, *130*, 17552−17562. (c) Dote, H.; Kaneko, M.; Inoue, K.; Nakashima, S. Synthesis of anion-mixed crystals of assembled complexes bridged by 1,2,-bis(4-pyridyl)ethane and ligand field of Fe(NCS)(NCBH₃) unit. *Bull. Chem. Soc. Jpn.* **2018**, *91*, 71−91.

(39) Neville, S. M.; Halder, G. J.; Chapman, K. W.; Duriska, M. B.; Southon, D.; Cashion, J. D.; Létard, J.-F.; Moubaraki, B.; Murray, K. S.; Kepert, C. J. Single-crystal to single-crystal structural trans-

formation and photomagnetic properties of a porous iron(II) spin-crossover framework. *J. Am. Chem. Soc.* **2008**, *130*, 2869−2876.

(40) Romero-Morcillo, T.; De la Pinta, N.; Callejo, L. M.; Piñeiro-López, L.; Muñoz, M. C.; Madariaga, G.; Ferrer, S.; Breczewski, T.; Cortés, R.; Real, J. A. Nanoporosity, inclusion chemistry, and spin crossover in orthogonally interlocked two-dimensional metal−organic frameworks. *Chem. - Eur. J.* **2015**, *21*, 12112−12120.

(41) Dolomanov, O. V.; Bourhis, L. J.; Gildea, R. J.; Howard, J. A. K.; Puschmann, H. OLEX2: a complete structure solution, refinement and analysis program. *J. Appl. Crystallogr.* **2009**, *42*, 339−341.

(42) Mariette, C.; Trzop, E.; Mevellec, J.-Y.; Boucekkine, A.; Ghoufi, A.; Maurin, G.; Collet, E.; Muñoz, M. C.; Real, J. A.; Toudic, B. Symmetry breakings in a metal organic framework with a confined guest. *Phys. Rev. B* **2020**, *101*, No. 134103.

(43) Sheldrick, G. M. Crystal Structure Refinement with SHELXL. *Acta Crystallogr. Sect. C: Struct. Chem.* **2015**, *71*, 3−8.